Cement and Concrete Research 41 (2011) 696–710

Contents lists available at ScienceDirect

Cement and Concrete Research

journal homepage: http://ees.elsevier.com/CEMCON/default.asp

The study of disorder and nanocrystallinity in C–S–H, supplementary cementitious materials and geopolymers using pair distribution function analysis

Cagla Meral [a], C.J. Benmore [b], Paulo J.M. Monteiro [a,*]

[a] Department of Civil and Environmental Engineering, University of California, Berkeley, California 94720, USA
[b] X-ray Science Division, Argonne National Laboratory, 9700 S. Cass Avenue, Argonne, Illinois 60439, USA

ARTICLE INFO

Article history:
Received 17 March 2011
Accepted 31 March 2011

Keywords:
B: amorphous material
Calcium–Silicate–Hydrate (C–S–H)
X-ray diffraction
C: alkali-aggregate reaction
Geopolymer

ABSTRACT

Significant progress was achieved with the application of Rietveld method to characterize the crystalline phases in portland cement paste. However, to obtain detailed information on the amorphous or poorly crystalline phases, it is necessary to analyze the total scattering data. The pair distribution function (PDF) method has been successfully used in the study of liquids and amorphous solids. The method takes the Sine Fourier transform of the measured structure factor over a wide momentum transfer range, providing a direct measure of the probability of finding an atom surrounding a central atom at a radial distance away. The obtained experimental characteristic distances can be also used to validate the predictions by the theoretical models, such as, molecular dynamics, *ab initio* simulations and density functional theory. The paper summarizes recent results of PDF analysis on silica fume, rice husk ash, fly ash, ASR gel, C–S–H and geopolymers.

Contents

1. Introduction

In this issue of *Cement and Concrete Research*, Bellmann and Stark review the state of the art in the field of cement hydration and microstructure analysis. Our paper presents the fundamentals of total scattering methods and explores how this powerful tool can be used in cement and concrete research to characterize amorphous and poorly crystalline phases. As examples, pair distribution function (PDF) analyses are applied to silica fume, fly ash, rice husk ash, ASR (alkali silica reaction) gel, C–S–H and geopolymers.

In the last century, the ability to determine the atomic structure of complex materials increased exponentially. Study at the atomistic level, which is essential to understanding the basic properties of a material, provides researchers with the tools to create solutions to pressing problems that have previously been dealt with on an *ad hoc* basis because of a fundamental lack of knowledge regarding simple material mechanisms. The periodicity, extended symmetry, and long-range order (LRO) of crystalline materials provided the basis for the development of systematic and quantitative structural analysis methods [1]. Starting from mid-1930 s, x-ray diffraction has been used for quantitative phase analysis of crystalline materials. In the 1970 s, the ground-breaking Rietveld method [2] opened a new, exciting chapter in refinement of crystalline structures. Method uses the whole profile of the powder diffraction pattern, and utilizes the

* Corresponding author. Tel.: +1 510 643 8251; fax: +1 510 643 5264.
E-mail address: monteiro@berkeley.edu (P.J.M. Monteiro).

0008-8846/$ – see front matter © 2011 Elsevier Ltd. All rights reserved.
doi:10.1016/j.cemconres.2011.03.027

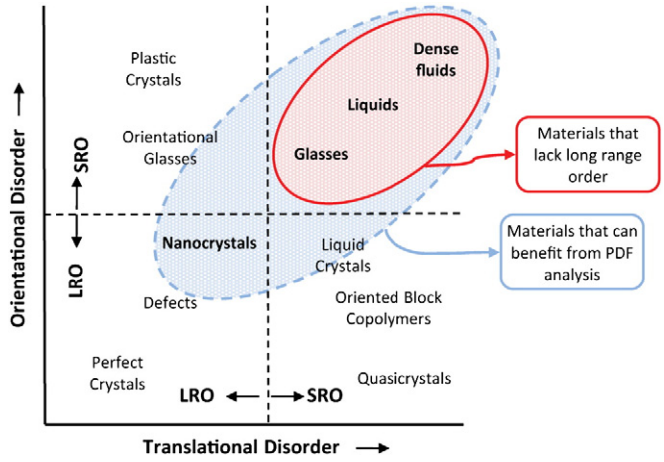

Fig. 1. Schematic plot of translational and orientational order and disorder in materials, adapted from [101]. LRO, long range order. SRO, short range order.

unit-cell dimensions for determining the peak positions, and the atomic positional and thermal displacement parameters as a model for the peak intensities [3]. The details of using the Rietveld method to characterize anhydrous cements and hydrated cement paste can be found in [4,5]. The main limitation of traditional structure refinements is the fact that they yield only long-range average structures of the material but neglect the diffuse scattering part of the diffraction pattern, which contains information on the local disorder [6]. In contrast to crystalline solids, structurally disordered materials (Fig. 1) lack long-range periodic order, and yet, their structure is not random. They still contain significant and varied local atomic structural motifs on the length scales up to several tens of nearest neighbors [7]. Their lack of long-range order (LRO) severely restricts the utility of traditional structure refinement methods.

Experimental determination of the complete atomic structure of an amorphous (*i.e.* glasses and liquids) or a poorly crystalline (*i.e.* nanocrystals, and gels) material is nearly impossible, as it would require a precise determination of the coordinates of all of the atoms. Material properties are not determined by the absolute position of each atom, but by the relative positions of the atoms which are close enough to interact [8]. Therefore, the knowledge of the local atomic environment and the relative positions of near neighbor atoms is extremely valuable both for an amorphous and a nanocrystalline material.

Neutron and x-ray diffraction techniques measure the differential scattering cross-section (see Fig. 2). The measurements are generally represented in momentum transfer (Q) space, or commonly known as reciprocal space. Q, the momentum transfer vector, is the difference between the wave vectors of the incident and scattering neutrons or

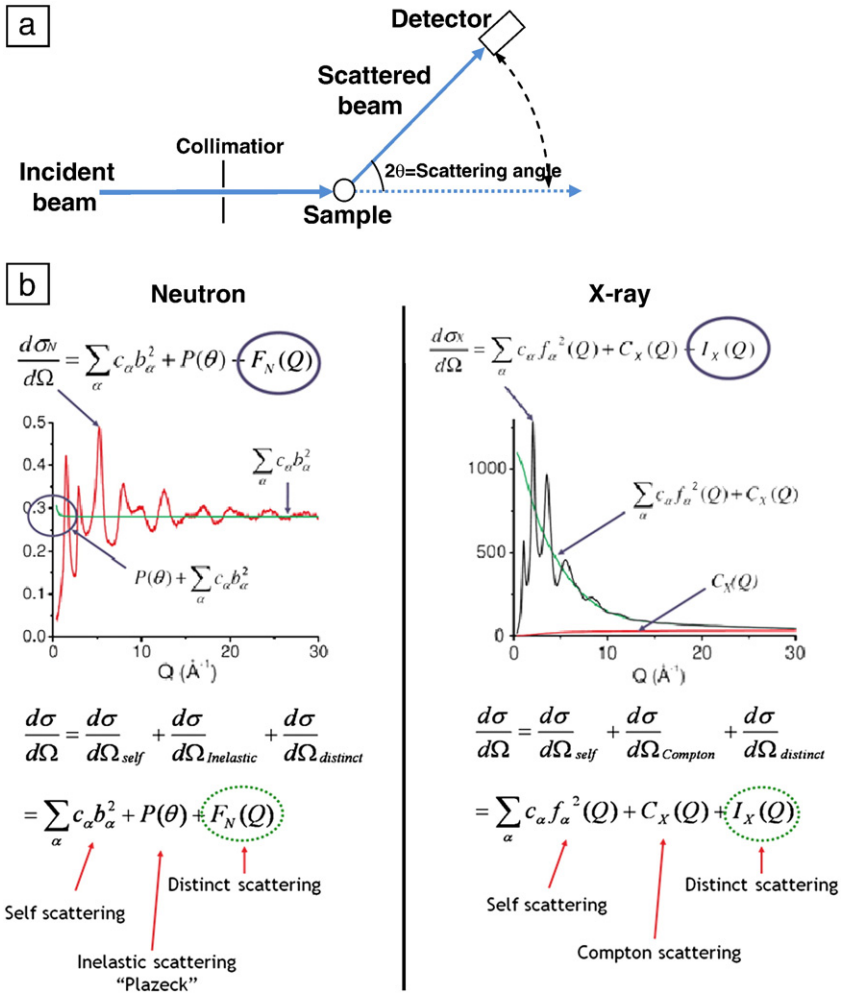

Fig. 2. (a) Schematic for a typical scattered intensity from a sample using a monochromatic incident beam. (b) Examples of spallation neutron and x-ray differential scattering cross sections, $d\sigma/d\Omega$, where Q is the momentum transfer vector, c_α is the atomic concentration of atoms of species α, b_α is the coherent neutron scattering length, $f_\alpha(Q)$ is the x-ray (usually atomic) form factor for species α.

x-rays. For elastic scattering, the magnitude of Q is given by $4\pi \sin\theta/\lambda$ where λ is the wavelength, and 2θ is the angle of scattering. The maximum experimental Q-range is limited to $4\pi/\lambda$, since $\sin\theta \leq 1$. For example, Cu K_α radiation, having a wavelength of 1.54 Å, has a Q-range limit of about 8 $Å^{-1}$ [8]. High energy synchrotron sources, such as Advanced Photon Source, USA, use wavelengths around 0.1 Å, allowing a dramatically wider Q-range compared to a standard laboratory x-ray diffraction instrument using Cu K_α radiation.

The differential scattering cross-section is proportional to the structure factor, S(Q), of a monatomic system, or to a weighted sum of partial structure factors, $S_{\alpha\beta}(Q)$, for a polyatomic system, as shown in Fig. 3 [9]. For example, vitreous germania (GeO_2) has three partial structure factors, namely Ge–Ge, Ge–O and O–O (see Fig. 3-b). By identifying each species or element specific group of the contributing atom–atom correlations explicitly, the x-ray weighted total structure factor can be written as:

$$\mathbf{S_X}(\mathbf{Q}) - 1 = \sum_{\alpha,\beta=1}^{\mathbf{n}} \mathbf{c_\alpha c_\beta f_{\alpha\beta}}(\mathbf{Q}) \left[\mathbf{S_{\alpha\beta}}(\mathbf{Q}) - 1\right] \quad (1)$$

$$= \rho_0 \sum_{\mathbf{i}=1}^{\mathbf{n}} \mathbf{c_\alpha c_\beta f_{\alpha\beta}} \int_0^\infty 4\pi \mathbf{r}^2 \left[\mathbf{g_{\alpha\beta}}(\mathrm{r}) - 1\right] \frac{\sin \mathbf{Qr}}{\mathbf{Qr}} \mathbf{dr}$$

where $\rho_o = N/V$ is the atomic number density (in atoms/$Å^3$), c_α is the atomic concentration of atoms of species α, $S_{\alpha\beta}(Q)$ are the partial structure factors, $g_{\alpha\beta}(r)$ are the corresponding partial pair distribution functions, r is the distance in real space and

$$\mathbf{f_{\alpha\beta}}(\mathbf{Q}) = \mathbf{f_\alpha}(\mathbf{Q}) \mathbf{f_\beta}(\mathbf{Q}) / \sum_{\alpha=1}^{\mathbf{n}} \mathbf{c_\alpha f_\alpha^2}(\mathbf{Q}) \quad (2)$$

where $\mathbf{f}_\alpha(Q)$ is the real x-ray form factor for atomic species α [10]. When neutrons are used, $\mathbf{f}_\alpha(Q)$ is replaced by the Q-independent coherent neutron scattering length, b_∞ [10]. The interactions of neutrons and x-rays with matter are very different. X-rays are more sensitive to heavier elements (*i.e.* have a higher Z value); whereas the neutron cross-sections tend to be more similar, displaying variation from isotope to isotope in a complex pattern. Therefore, combining neutron and x-ray diffraction techniques often provides complementary information [9]. A review of notations for representing S(Q) in terms of distribution functions is given in [11].

In order to obtain an accurate S(Q), a multitude of experimental effects need to be minimized and/or corrected for (container scattering, sample absorption, multiple scattering, detector efficiency, etc.) before normalization. There are various computer programs available for these x-ray and/or neutron specific corrections, depending on the type of measurement. For example PDFgetX2 is commonly used for analysis of x-ray PDF measurements [12]. A summary of data treatment and corrections for neutron PDF scattering measurements of liquids and glasses can be found in [13].

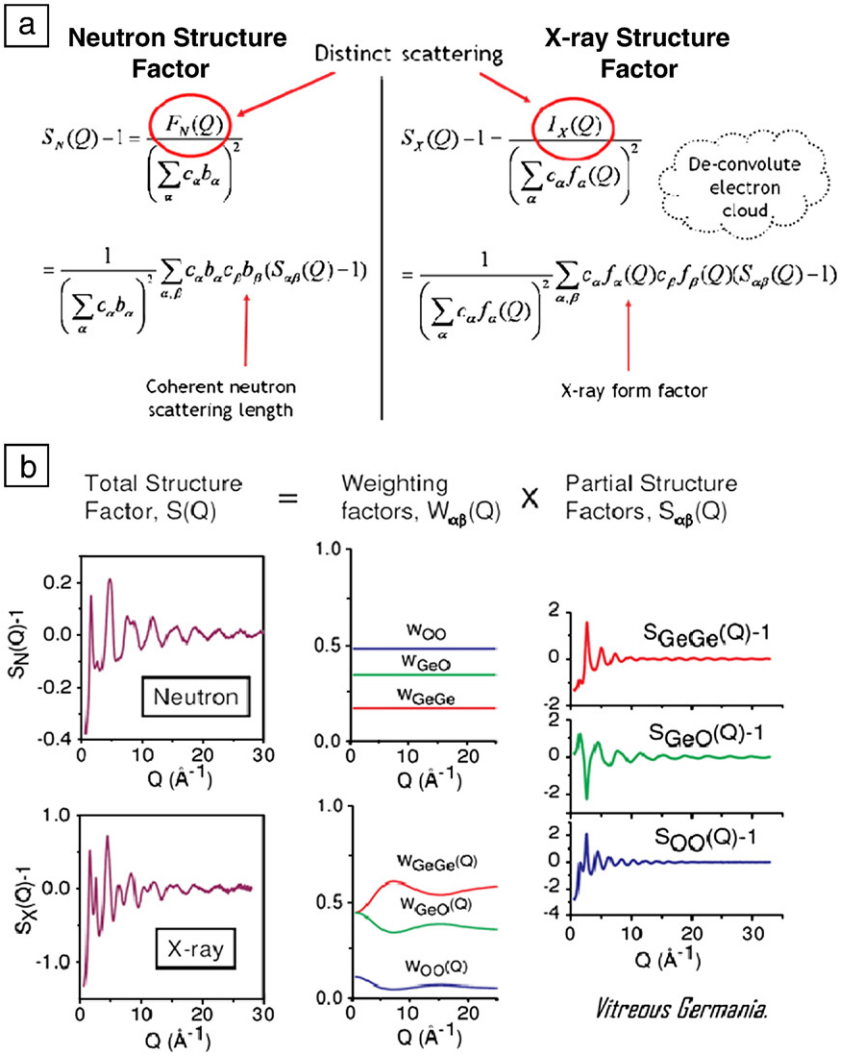

Fig. 3. (a) Neutron and x-ray structure factors, S(Q). (b) Partial neutron and x-ray structure factors for vitreous germania [42].

S(Q) can be directly studied in reciprocal space; because the low-Q peaks are highlighted in this representation and are dominated by intermediate or extended range ordering, whereas the high-Q oscillations are primarily related to the local bond distributions. However, the local structure is more easily visualized by (partial) Fourier transforming S(Q) into real space and studying the (total or partial) pair-distribution functions (PDF) (see Fig. 4). As in structure factors, for a material containing n different atom types, there are $n(n+1)/2$ partial PDFs contributing to the measured total, each weighted by the concentration and scattering strength of the involved pair of species.

Theoretically, the integral in the transformation is performed over the range from zero to infinity, but in practice, the finite value of maximum accessible Q_{max} in the Sine-Fourier transform leads to peak broadening and non-physical oscillations (also called truncation ripples) at low-r values in real space [14]. This can be minimized by damping S(Q) at high-Q values (e.g. by Lorch modification function [15]) before the Fourier transformation. The total x-ray pair distribution function, $G_X(r)$,

$$G_x(r) = \frac{f_\alpha(Q)f_\beta(Q)}{(2\pi)^3\rho_0}\int_0^\infty 4\pi Q^2 S_X(Q)\frac{\sin Qr}{Qr}dQ \quad (3)$$

represents the weighted sum of the partial PDFs, $g_{\alpha\beta}(Q)$, emphasizing the local structural correlations and is commonly used in the studies of liquids and computed as an output from Molecular Dynamics or Monte Carlo simulations [16]. In calculations, both the sharp Bragg peaks (as a result of LRO), and diffuse components (as a result of disordered local structure) are taken into consideration. Therefore, the PDF method is also referred to as the total scattering method.

It is sometimes useful to emphasize the medium- or long-range correlations by using the differential distribution function, $D_x(r) = 4\pi r\rho_0(G_X(r)-1)$, [10]. Also, the representation $N_x(r) = rT_x(r) = 4\pi r^2\rho_0 G_X(r)$ has a direct physical interpretation to actual coordination numbers, since $N(r)d(r)$ represents the number of atoms lying within a range $(r+dr)$ from any given atom [9].

The PDF technique was pioneered by Warren [17] in the 1930 s using x-rays to study non-crystalline forms of matter. However, it gained popularity first in the field of neutron scattering – especially in the 1980 s – with the development of high flux spallation neutron sources, providing access to high momentum transfers. With the development of 3rd generation synchrotrons in the mid-1990s and the production of hard x-ray beams, PDF analysis using high energy x-rays began to enjoy equal footing with neutron diffraction experiments as a research tool for studying disordered materials. During this time, PDF was increasingly applied to characterize nanocrystalline systems as well as amorphous and liquid materials.

In a PDF experiment utilizing an x-ray probe, a monochromatic beam of high energy x-rays (>60 keV) scatters in transmission geometry, passing through the sample into a detector in the forward direction (see Fig. 2-a). The combination of high energy and low angle compresses a wide momentum transfer (Q) range into a small angular solid angle, minimizing attenuation and multiple scattering effects on millimeter-

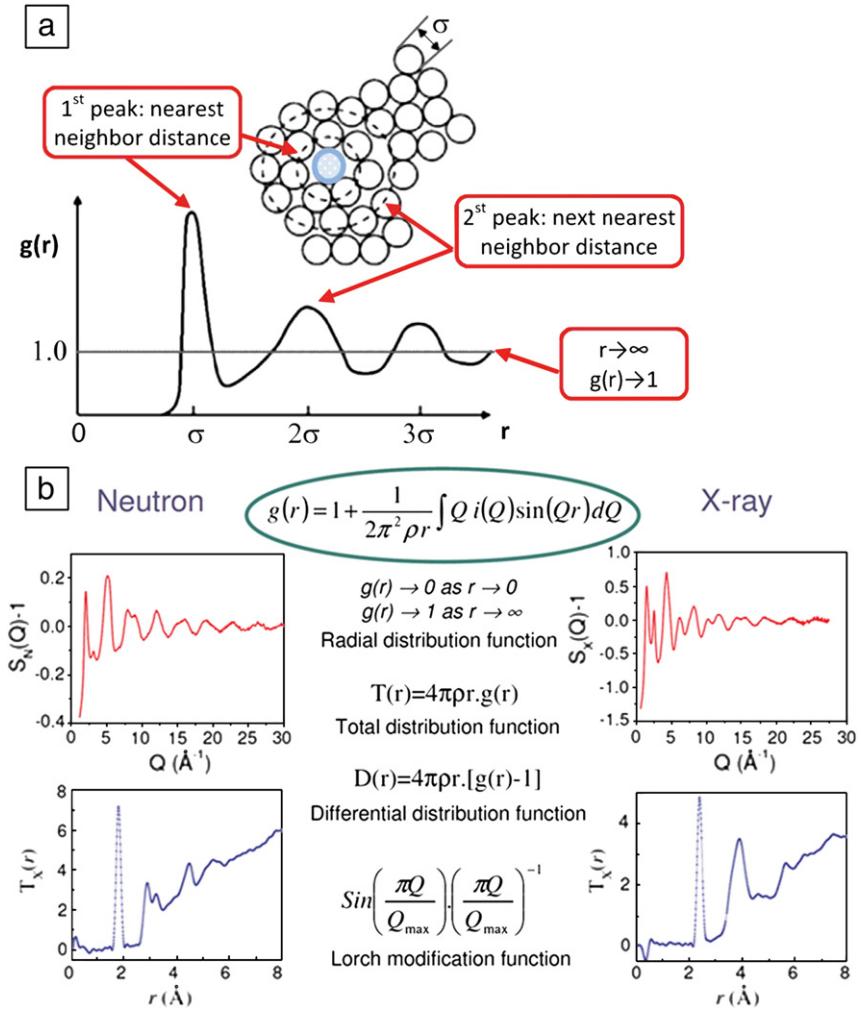

Fig. 4. (a) Pair distribution function, G(r), for a monatomic system. G(r) allows us to visualize the probability of finding another atom at a given distance r in real space, adopted from [102]. (b) Calculating G(r) from S(Q) for neutrons and x-rays.

sized samples. Today, there is a handful of high energy x-ray PDF beamlines around the world and a large boost to the versatility of this technique has been the use of large area detectors, which allow for much shorter measurement times but lack energy discrimination. For example, the high energy x-ray beamline at 11-ID-C at the Advanced Photon Source, USA operates at 115 keV and has three pairs of horizontal and vertical collimating slits (see Fig. 5). An ion chamber measures the incident flux and the direct beam that is not scattered or absorbed by the sample. The incident beam is blocked with short length of 3 mm diameter tungsten rod, mounted in front of the area detector. The sample is positioned on a goniometer with three-dimensional motor control. Alignment is initially performed using an optical telescope and laser beam system, and precise adjustments (to within 10 μm) are made using the x-ray beam and a moveable photodiode detector. Regular dark current measurements are performed between area detector scans to minimize the effects of electronic drift. To capture structural changes upon vitrification or crystallization, rapid scans on aluminosilicate melts have been performed as fast as every 200 ms. For accurate local and intermediate range order structure determination, however, count times of 20–30 min are more common on cementious materials on 11-ID-C to provide good statistics over a wide Q-range.

The PDF method is most powerful when interpreted along with information from other methods, both experimental and computational. Partial structure factor information may be extracted by using both x-ray PDF and neutron PDF data sets together, and also through the techniques of anomalous scattering, isomorphic substitution and isotopic neutron diffraction substitution experiments [9,18]. Combining PDF data with x-ray or neutron small angle scattering, nanotomography, high-resolution TEM, or reflectivity measurements is very useful to interpret the collected data [19]. Although these methods do not provide any atomic structure information, they give important supplementary data such as particle size, density fluctuations and homogeneity of the sample.

PDF gives an overview of the structure of the material over a wide range of length-scales and places strong constraints on any atomistic model. Widely used methods to model PDF data are Reverse Monte Carlo (RMC) modeling [20], and Empirical Potential Structural Refinement (EPSR) [21]. The RMC method iteratively refines a three-dimensional atomistic model of the material that is consistent with PDF data sets [9], analogous to a Rietveld refinement in crystallography. An important advantage of using RMC modeling is its flexibility in combining different data types into the same model. The main disadvantage of this (or any similar) technique is the lack of a unique structure solution. Additionally, in RMC modeling the starting configuration has to be chosen carefully, since the method lacks inherent chemical and thermodynamic constraints. EPSR is, in concept, a similar method compared to RMC or Rietveld refinement, targeting mainly molecular systems, whereby it refines an interatomic potential until the three-dimensional atomic model for the system is in agreement with the PDF data [21].

Classical molecular dynamics (MD) predict the PDF by moving atoms in a limited simulation box according to predefined interatomic potentials and force fields. The used potentials are often derived from known crystal structures and do not always represent the investigated system. MD simulations do not always reproduce the S(Q) data precisely. However, they predict trends well, as information on both structure and dynamics of the system as chemical bonding information is assigned to atoms.

Ab initio molecular dynamics simulations combine the advantages of MD and density functional theory, and generally provide more accurate models than MD simulations with the added cost of computational time. Simulations on disordered materials usually require thousands of atoms for useful statistical averaging and information on intermediate range ordering. This large requirement prevents the application of *ab initio* MD simulations in many cases.

The two most common x-ray absorption methods, the extended x-ray absorption fine structure (EXAFS) and the x-ray absorption near-edge structure (XANES), are also used in combination with PDF data. EXAFS is an element-specific bulk probe that is sensitive to dilute species. EXAFS reveals information about the ligation, coordination number and bond distance in the local molecular environment of the investigated element [9,19]. The information obtained from EXAFS complements PDF analysis. XANES, similar to EXAFS, provides only near neighbor distance distributions and coordination numbers, but it is much more sensitive to bond angles compared to EXAFS [19]. In cement research, most of the applications of EXAFS and XANES are in the study of immobilization of species by the hydration products [22–24].

Raman spectroscopy in solids utilizes the inelastic or Raman scattering of monochromatic light usually from a laser. The extreme sensitivity of Raman spectra to local deviations from the average

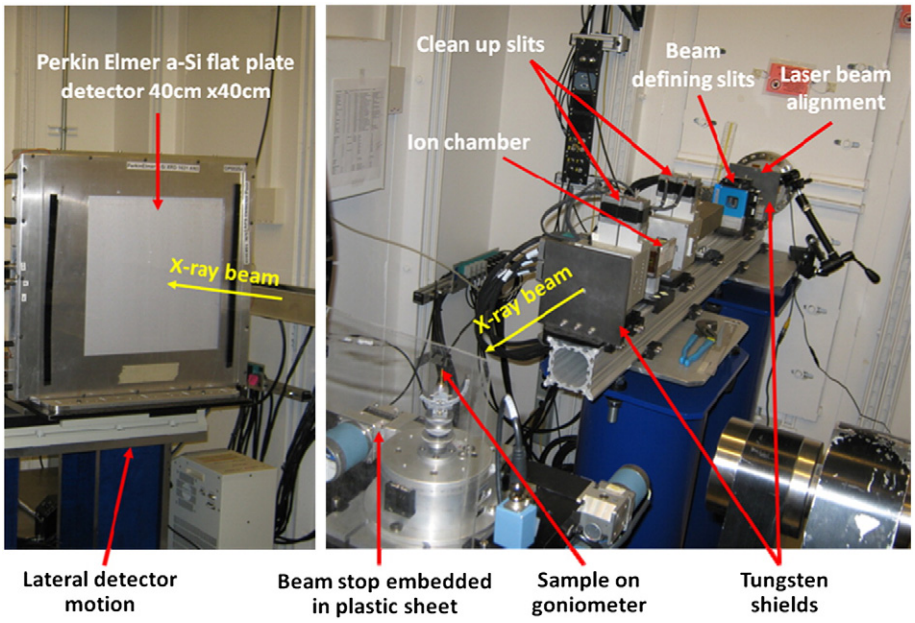

Fig. 5. Beamline 11-ID-C, advanced photon source, USA. Fixed incident energy 115 KeV (wavelength 0.108 Å).Sample-detector distance: 25–300 cm; Q-range: 0.2–40 $Å^{-1}$; detector pixel size: 0.2 mm × 0.2 mm.

periodicity makes it valuable in exploring local structure [19], providing supplementary information for PDF analysis. Recent applications of Raman spectroscopy to study calcium–silicate–hydrates (C–S–H) have been reported by Garbev et al. [25] and Black et al. [26]. Solid state NMR is another powerful technique that could be used in combination with PDF analysis. It is sensitive to local structure in disordered materials and yields information on local symmetry and the speciation distribution of the probe atom [27,28], whereas PDF only gives average coordination numbers.

2. Characterization of supplementary cementitious materials with PDF

The global production of portland cement is 2.8 billion ton per year [29] and considering a global average clinker factor of 0.8 ton of clinker per ton of portland cement [30,31], the annual CO_2 emissions from cement production reach almost 2.2 billion metric tons, constituting more than 6% of the global atmospheric emissions [32]. The use of supplementary cementitious materials (SCMs) is an attractive option to reduce the amount of portland cement in a given concrete mixture proportion and to produce durable environmentally benign materials. Power plants using coal as fuel, and metallurgical furnaces producing cast iron, silicon metal, and ferrosilicon alloys are the major sources of SCMs. Currently the global availability of fly ash, a byproduct from coal combustion, is between 550 and 610 million tons [33,34] but not all of it is suitable for use in cements and concrete mixtures. The global availability of granulated blast-furnace slag, a byproduct from pig iron production, while more widely used than fly ash, is of the order 200 million tons [35]. Other SCMs include natural pozzolans, silica fume, rice husk ash and metakaolin. The efficiency of a SCM depends on its chemical composition, fineness and amount of amorphous phases. Lothenbach et al. [36] provided a comprehensive review of the effect of SCMs on the microstructure and hydration kinetics; the present paper analyses the amorphous phase of silica fume, rice husk ash, fly ash and metakaolin using total scattering methods.

2.1. Amorphous silica, silica fume and rice husk ash

Silica glass is a continuous network made of corner sharing SiO_4 tetrahedra where each oxygen bridges two tetrahedra (*i.e.* only Q^4 speciation). A schematic 2D Zachariasen [37] model for pure silica glass is given in Fig. 6-a. However, a more complex system might contain 75% Q^3 (tetrahedra with one free non-bridging oxygen), 25% Q^2 (two non-bridging oxygens). Fig. 6-b illustrates x-ray and neutron scattering measurements on silica glass (data from [18]). The most noticeable difference in the x-ray and neutron measurement is the appearance of the Q_2 peak in the neutron spectrum which arises from O–O interactions. For silica glasses, the first diffraction peak, Q_1 (Fig. 6-b), has been associated with intermediate range ordering with a periodicity of $2\pi/Q_1 \sim 6$ Å. This ordering beyond the first few nearest neighbor tetrahedra arises from the boundaries between successions of cages comprising the structure of a 3-D covalent network [7]. Therefore, the position and shape of the first sharp diffraction peak Q_1 can provide information on different sized ring distributions within the material. The second diffraction peak at position Q_2 has been linked to chemical or extended range ordering with a periodicity of $2\pi/Q_2 \sim 3$ Å and the local Si–O–Si and O–Si–O bond-angle distributions can persist to distances as large as >5 Å [10,18]. The similar features in $S_N(Q)$ and $S_X(Q)$ at higher Q-ranges are dominated by the SiO_4 tetrahedra present in the glass. The total neutron and x-ray pair distribution functions for silica glass are given in Fig. 6-c. As expected, x-rays and neutrons produce different total pair-distribution functions. Si and O partials are weighted similarly for x-rays since Si is the predominantly scattering atom, but there are twice as many oxygens; and O dominates the spectra for neutrons, since O has a larger neutron cross section and is more abundant. Therefore, the Si–Si interactions, and hence the Si–O–Si bond angle, is best obtained from the x-ray data whereas the O–O interactions and the O–Si–O bond angle are best studied with neutron data [7].

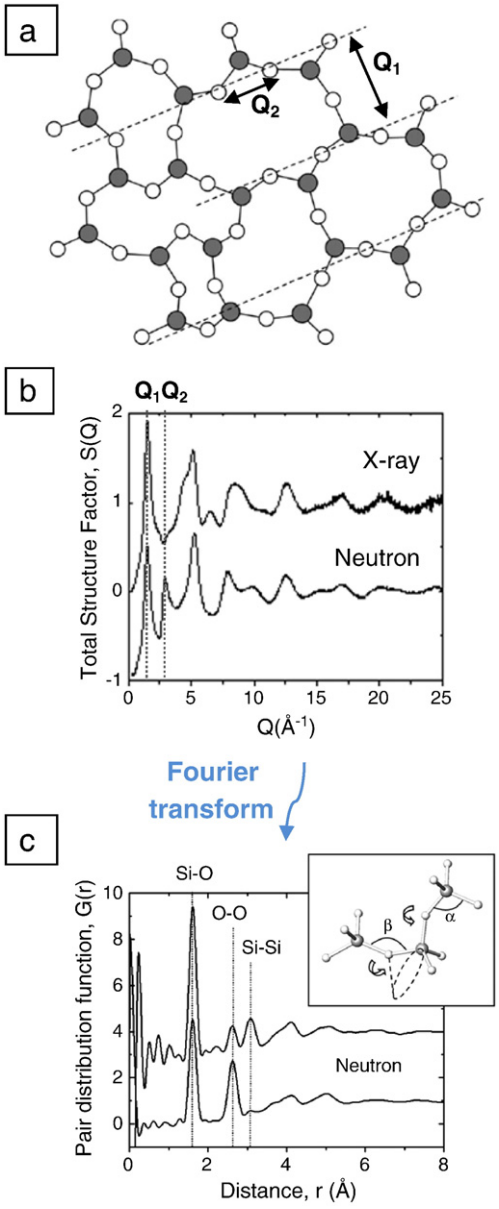

Fig. 6. (a) 2-D representation of Zachariasen [37] — Wright [7] continuous network model for a glass structure with corner-sharing tetrahedral oxides (*i.e.* Si atoms, ●, and O atoms, o) (adapted from [18]). The dashed lines of periodicity (Q_1) arise from correlations between cages which comprise the glassy silicate network. Q_2 represents the length scale of the bulk chemical ordering of the network. (b) Measured x-ray and neutron total structure factors for glassy SiO_2 [10]. Q_1 is the first sharp diffraction peak. (c) The total x-ray and neutron radial pair distribution functions for vitreous SiO_2. The inset shows the local tetrahedral and packing torsion angles [10].

Silica fume, a byproduct from the induction arc furnaces used in the silicon metal and ferrosilicon alloy industries, is a highly pozzolanic material. The SiO vapors, produced by the reduction of quartz to silicon, oxidize and condense in the low-temperature zone of the furnace to form very small spherical particles consisting of noncrystalline silica. The material removed by filtering the outgoing gasses in bag filters has an average diameter on the order of 0.1 μm. Rice husk ash, another highly pozzolanic material is produced by the controlled combustion of rice husks (shells produced during the dehusking operation of paddy rice) [38,39]. Each ton of paddy rice generates about 200 kg of husk and upon on combustion of these, it is

possible to yield approximately 40 kg ash. Folliard and Mehta [40] provided a careful study of the durability of concrete mixtures containing rice husk ash. ^{29}Si MAS NMR measurements [41] on rice husk ash showed that if the husk is burned in a controlled temperature, the resulting ash contains only SiO_4 tetrahedral units.

The measured x-ray total structure factors for silica fume and rice husk ash with silica glass are given in Fig. 7-a. The Q_1 positions (and widths relating to coherence) are same for all amorphous silicas, suggesting a similar intermediate range ordering with a periodicity of $2\pi/Q_1 \sim 6$ Å. Fig. 7-b provides the breakdown of the total x-ray pair distribution function, $G_X(r)$, for glassy SiO_2 in terms of its partial distribution functions, $g_{\alpha\beta}(Q)$. Utilizing this knowledge, the near neighbor correlations in Fig. 7-c and Fig. 7-d can be labeled. Si_1–O_1 distance is found to be ~1.62 Å which is an indication for SiO_4 tetrahedra based on comparison to crystallographic ionic radii. The O_1–O_1 distance of 2.62 Å provides an O–Si–O angle of ~109°. The measured 3.08 Å Si_1–Si_2 distance is robust and provides an indication of the average ring size. For both samples Si_1–O_2, O_1–O_2, bond lengths are observed as 4.11 Å, and 5.04 Å, respectively. These values are very similar to that of a silica glass, suggesting similar topology (related with distribution of n-sized rings) of silica fume and rice husk ash to silica glass network. Silica glass is known to have a wide distribution of ring sizes with n = 6 being the most common, but also a significant amount of n = 4, 5, 7 and 8 membered rings present [42].

2.2. Fly ash

It is common practice to incorporate 15–25wt.% of fly ash in concrete mixture. However, in recent years there has been increased interest in developing high-volume fly ash (HVFA) concrete systems as a powerful means by which concrete structures can be built in a more resource-efficient manner than those made of conventional portland-cement concrete [43]. Fly ash is also an important raw material for the production of geopolymers (see Section 5). To optimize fly ash, it is critical to characterize the amorphous reactive phase.

In the present paper, special emphasis is given to the characterization of the aluminosilicate glass obtained from fly ash-F since it was used as a controlled raw material for the geopolymer sample to be described in Section 5. The details of phase separation process are explained in [44]. The chemical composition of the fly ash glass is given in Table 1. The main incentive behind using phase separation was to generate a more uniform raw material, increase the geopolymerization rate and homogeneity of the resulting product.

Amorphous aluminosilicates are among the most important binary systems for the earth sciences and materials sciences. Therefore, they have been studied in great detail with experiments and computer simulations. The local charge neutrality in aluminosilicates require Al^{3+} ions to have a different O^{2-} ion environment from that of Si^{4+} ions [45]. Unlike the continuous network of SiO_2 tetrahedra, Al^{3+} ions on their own do not form a network of AlO_4 tetrahedra. A wide range of experiments such as NMR [46–48], IR and Raman spectroscopy [49], and x-ray scattering [49] suggested a relatively large amount of 4-, 5- and 6-fold Al atoms and 3-fold O atoms in aluminosilicate glasses. Sen et al.'s NMR results [50] for aluminosilicate glasses with varying Al_2O_3 content showed that the fraction of highly coordinated Al atoms (*i.e.* 5- and 6-fold) units has a tendency to increase with increasing Al_2O_3 content.

The fly ash glass used in this study has an Al_2O_3/SiO_2 molar ratio around 0.25. MD simulation on amorphous $Al_2O_3.2SiO_2$ by Winkler et al. [51] suggested a distorted tetrahedral network in that Al and Si

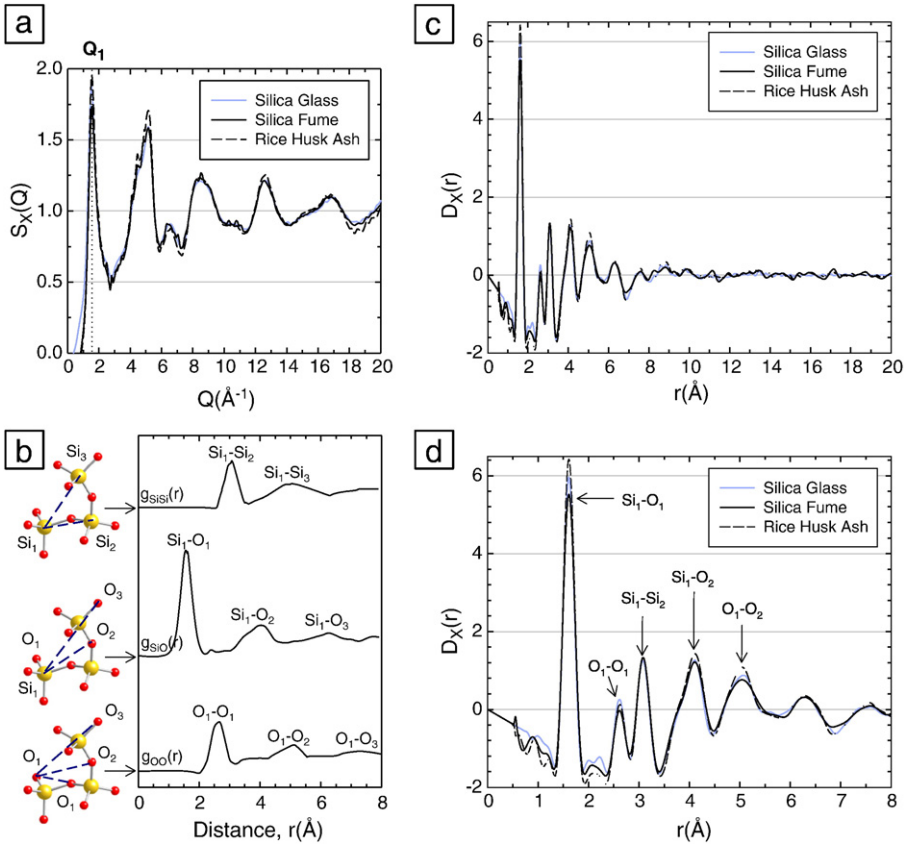

Fig. 7. (a) The measured x-ray structure factors, $S_X(Q)$, of silica fume and rice husk ash. (b) Faber-Ziman defined partial pair-distribution functions in terms of element specific contributions for SiO_2 glass: $g_{SiSi}(r)$, $g_{SiO}(r)$ and $g_{OO}(r)$. The peaks in the distribution functions are illustrated by the distances indicated in the atomistic plots of three corner shared SiO_4 tetrahedra [10]. (c–d) The x-ray differential distribution function $D_X(r)$. Peaks are labeled according to (b).

Table 1
Chemical composition (% mass) of the aluminosilicate glass separated from Class F coal fly ash and metakaolin.

Chemical composition (wt.%)		
	Fly ash F glass	Metakaolin
SiO_2	45.10	52.00
Al_2O_3	21.36	43.00
Fe_2O_3	4.81	2.00
K_2O	1.47	–
TiO_2	1.02	3.00
CaO	8.74	–
Na_2O	5.19	–
SO_3	5.19	–
MgO	3.49	–
MnO	0.09	–
LOI	3.54	–

are mainly 4-fold coordinated to oxygen. A snapshot of their $Al_2O_3.2SiO_2$ model at T = 300 K is given in Fig. 8-a. The same tendency was found for Al_2O_3–SiO_2 melts with 13 and 47 mol% Al_2O_3 [52] suggesting a similar case for fly ash glass. The packing of AlO_4 tetrahedra is very different from that of SiO_4 tetrahedra. This difference is explained by the presence of triclusters (*i.e.*, the unit where an O is surrounded by three cations, Al and Si atoms together) and edge-sharing AlO_4 tetrahedra [52]. A comparison of reduced structure factor of our experimental fly ash glass data (see Fig. **8**-b) to those obtained from simulations by Winkler et al. [51] ($Al_2O_3.2SiO_2$), and Pfleiderer et al. [52] ($65Al_2O_3.73SiO_2$), a resemblance is observed, although the presence of Bragg peaks shows that the experimental data also have crystalline phases.

Hoang et al. [45,53,54] deepened the investigations on amorphous $Al_2O_3.2SiO_2$ in a MD model containing 3025 particles under periodic boundary conditions with the Born–Mayer type pair potentials. Calculated total differential distribution function (see Fig. 8-c) agrees with our fly ash glass measurements rather well. The simulation also provided detailed partial pair distribution functions (see Fig. 8-d). These partial PDFs can be used to identify the correlations in our fly ash glass. The functions $g_{AlO}(r)$ are very similar to $g_{SiO}(r)$, but the former has a slightly broader, and weaker, first peak due to the presence of AlO_5 and AlO_6. Compared to the fly ash aluminosilicate glass with 1.63 Å, the first peak position of Hoang's simulation, 1.51 Å, is underestimated. The 3.2 Å peak is due to cation–cation interactions with a broad low-r contribution from the O–O correlations.

2.3. Metakaolin

The dehydroxylation of kaolinite ($Al_2Si_2O_5(OH)_4$), a crystalline layered structure, produces amorphous metakaolin ($Al_2O_3.2SiO_2$), an effective supplementary cementitious material for concrete. The calcination conditions of kaolinite to form metakakaolin has been studied in detail [55]. Sabir et al. [56] provided a critical review on the use of metakaolin and calcined clays as pozzolans for concrete.

The study of the transformation from kaolinite (crystalline) to metakaolin (amorphous) at the atomic level is complex. White et al. [57] utilized an iterative method alternating between least-squares real-space refinement with neutron pair distribution function data, and

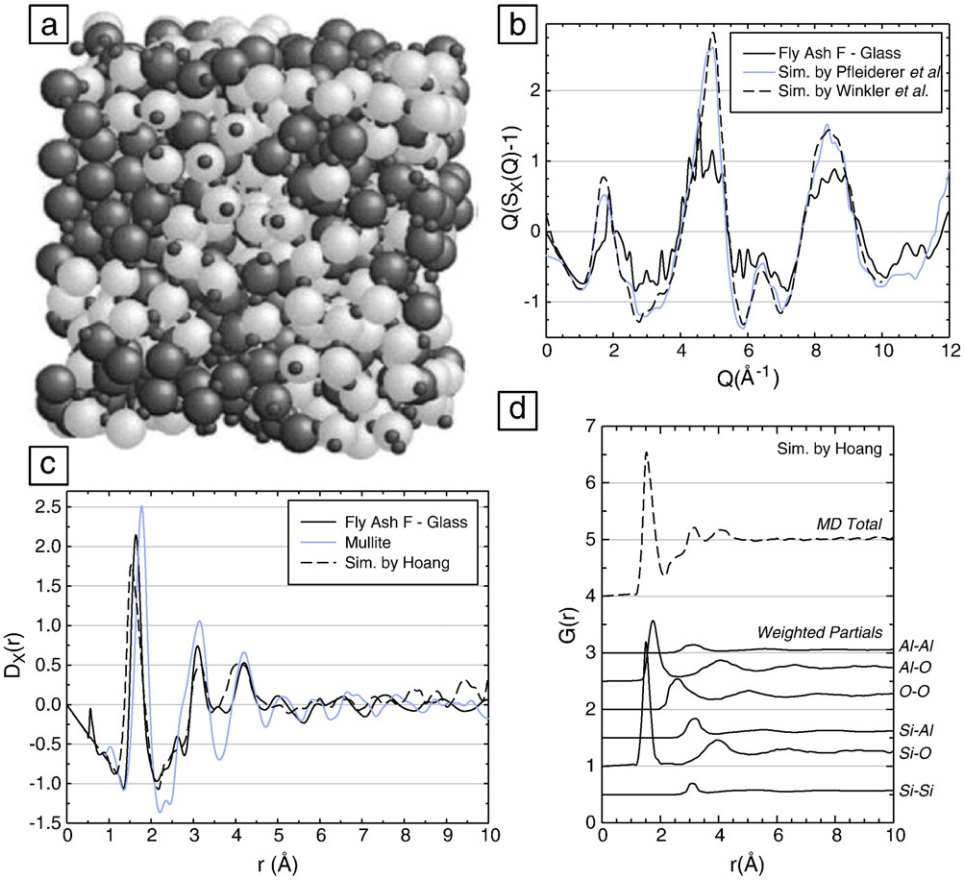

Fig. 8. (a) Snapshot for amorphous aluminum silicate $(Al_2O_3).2(SiO_2)$ at T = 300 K from Winkler et al. [51]. White spheres: Si; big black spheres: Al; small black spheres: O. The size of the spheres does not correspond to the actual size of the atoms. (b) Experimental reduced x-ray scattering structure factor $Q.(S_X(Q)-1)$ for fly ash F-glass in comparison with the simulation results by Winkler et al. [51] for $(Al_2O_3).2(SiO_2)$, and Pfleiderer et al. [52] for $65(Al_2O_3).73(SiO_2)$. (c) The experimental x-ray differential distribution function for fly ash-F glass compared to mullite $3(Al_2O_3).2(SiO_2)$ measurement, and Hoang's [45] molecular dynamics (MD) simulation for $Al_2O_3.2(SiO_2)$ melt. (d) The atom specific weighted partial differential distribution factors for Hoang's MD simulation [45].

energy minimization with density functional modeling to provide a better understanding of metakaolin structure. Their research reported that a) metakaolin was able to retain the original layering of kaolinite although the resulting layers are buckled locally and b) a small percentage of three-coordinated aluminum was present in metakaolin. In a later study [58], the authors applied the same methodology to systematically follow the dehydroxylation process of kaolinite into metakaolin.

Sperinck et al. [59] conducted MD simulations on a kaolinite super cell (4670 atoms) to gradually remove hydroxyls to obtain metakaolin. They reported a distortion or buckling effect in the Al–Si layers due to the migration of the aluminum into vacant sites in the interlayer spacing [59]. They followed the change in aluminum coordination from octahedral to tetrahedral, confirming the presence of 5- fold aluminum within the metakaolin structure similar to White et al. [58]. They did not observe 3-fold aluminum, and suggested that this might be due to the supercell allowing aluminum enough freedom to coordinate itself in the higher configurations that are inherently more stable.

3. Characterization of the alkali silica reaction gel with PDF

The alkali–silica reaction involves reactive siliceous aggregates with the highly alkaline concrete pore solution producing an alkali–silicate gel that can imbibe water and expand. If confined within the matrix, such expansion can possibly generate stresses that are large enough to crack the concrete. Double layer theory can provide a solid foundation to explain the expansion of ASR gels [60–62]. Hou et al.'s [63] detailed NMR investigation on synthetic and natural ASR gels suggested that the gel is an amorphous alkali (Na or K)–hydroxide–silicate glass with a Q^3-speciation dominant connectivity. Tambeli et al. [64] measured the mean number of non-bridging oxygens for the natural ASR gel to be around 1.0, a value much higher than the value of 0.51 for potassium-silicate glasses with the same K_2O content. This was explained by the depolymerization of the ASR gel due to the presence of a substantial number of hydroxyl groups. Wieker et al.'s [65,66] proposal that the ASR gel has a structure similar to Na or K silicate kanemite [(Na, K) HSi_2O_5:$3H_2O$] has been gaining acceptance. Kanemite has a layered structure of corrugated $[Si_2O_4OH]_n$ sheets and hydrated Na (or K) coordinated to six water molecules [67]. Benmore and Monteiro [10] recently compared the experimental x-ray PDF of the natural alkali silicate gel from Furnas Dam, Brazil with that obtained from the molecular dynamics (MD) simulation for amorphous Na-kanemite (Fig. 9). The x-ray PDF results were dominated by scattering from the Si and O atoms (due to their abundance and number of electrons) and showed some evidence of a layering with a periodicity of 9.7 Å. The local silicate structure was similar to the MD Kanemite model, but the experimental O–O peak was considerably broader such that the ordering only persisted over the length-scale of a few polyhedra. This suggests some revisions to the model are required.

We recently measured another natural K rich gel collected from Moxoto Dam, Brazil. The measured structure factor shows a low peak at $Q_1 = 0.65$ Å^{-1} similar to the Furnas Dam measurements. This small peak, corresponding to a periodicity of 9.7 Å, does not exist in a SiO_2 glass [18], or in a K–Si glass [68]. The relatively low intensity of this first peak at $Q_1 = 0.65$ Å^{-1} implies that the ordering of sheets does not persist much beyond a few layers in real space, see Fig. 10-a. A broad peak, much stronger than the Q_1 peak, can be found at $Q_2 = 1.85$ Å^{-1} associated with a periodicity of $2\pi/Q_2 \sim 3.4$ Å due to the chemical ordering of the bulk gel network [69,70]. The similarity of the structure factors of silica glass and Moxoto Dam at high-Q is due to the SiO_4 tetraheda dominating this region. The $S_X(Q)$ is Fourier transformed to obtain differential distribution function, $D_X(r)$ (see Fig. 10-b) with a Lorch modification function [15] to suppress for artifacts due to the finite measured Q-range. The obtained $D_X(r)$ shows a remarkable similarity to that from Furnas Dam gels [10].

The local structural correlations for Moxoto Dam gel are labeled in the light of the information obtained from with Furnas Dam gel and comparison with amorphous Na-Kanemite. Based on the detailed information on varying size polyhedra [71], and prior chemical knowledge of the gel, the peaks at 1.62 Å (Si_1–O_1) and 2.66 Å (O_1–O_2) in the measured spectra can be confidently assigned to the existence of SiO_4 tetrahedra. A K–O distance of ~2.78 Å is an indication of KO_6 octahedra. The KO_6 peak for our system is most likely hidden under the O–O peak as is in the Na-Kanemite MD simulation, Fig. 10-c. The

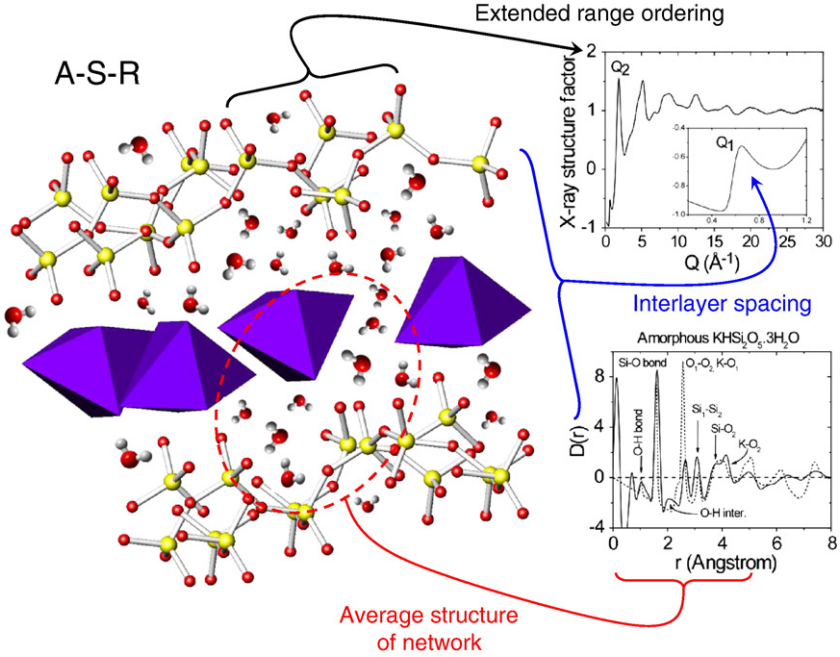

Fig. 9. (Left) A local structural model of the amorphous K-kanemite ($KHSi_2O_5$:$3H_2O$) gel consistent with the diffraction data by comparison to the ideal K-kanemite crystal structure [10]. (Right-top) The measured total x-ray structure factor for the amorphous K-kanemite gel from Furnas Dam [10]. (Right-bottom) The x-ray differential distribution function $D_X(r)$ for the Furnas Dam gel (solid line) compared to the MD Na-Kanemite model [67] (dashed line).

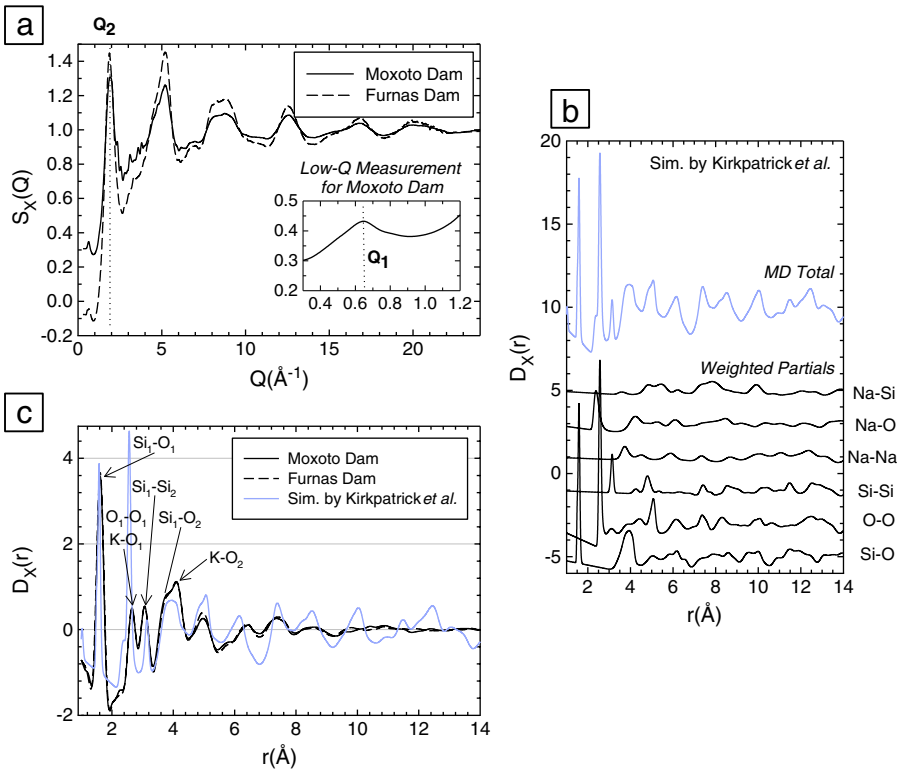

Fig. 10. (a) The measured total x-ray structure factor for Moxoto Dam. (Inset) Low-Q measurement focusing on Q_1. (b) Comparison of the experimental x-ray differential distribution functions $D_X(r)$ for ASR gels from Moxoto Dam (solid line) and Furnas Dam (dashed line) to amorphous Na-Kanemite simulation by Kirkpatrick et al. [10] (blue). Plots are offset for visibility. (Blue and dashed lines are scaled down with 0.5.) (c) The atom specific weighted partial differential distribution factors for the amorphous Na-kanemite simulation [10].

difference in the first nearest neighbor oxygen–oxygen (O_1–O_2) peaks of the simulation and the Moxoto Dam gel measurement is substantial. The measured peak is much smaller and broader indicating that the silica tetrahedra are considerably more distorted than the MD model predicts. This suggests a more disordered network structure beyond the distance of a few interconnected polyhedra supporting previously found results of Benmore and Monteiro [10]. The following peaks 3.08 Å (Si_1–Si_2), a low-r shoulder at 3.8 Å (Si_1–O_2) and a larger peak at 4.13 Å (K–O) is identified as other dominant correlations in Fig. 10-b. When compared with the simulation results, the measured higher-r peaks are notably smaller and broader with multiple contributions. No distinct structural correlations can be observed beyond ~10 Å. These findings support that ordering persists within only a lengthscale of four or five polyhedra as is the case for the gel from Furnas Dam. The 4.97 Å peak is carefully compared with MD simulation. In the simulation, the 5 Å peak has two contributions; the Si_1–Si_3 at 4.8 Å and the O_1–O_2 at 5.08 Å. This implies that the average orientations of the second and third nearest neighbor SiO_4 tetrahedra are much more disordered than those in the regularly aligned corrugated crystalline sheets, and this may allow some water molecules to penetrate the silicate layers [10].

The PDF analysis results on Moxoto Dam gel are consistent with MD simulation findings [63] suggesting that the water penetration to the interlayer volume in significant quantity is not energetically favorable, and that for the large expansions observed in the gel, a continuous polymerized silicate layer is unlikely. The distorted kanemite-like structure seems to be a good starting structure; however the PDF data also indicates a need to refine this model. Benmore and Monteiro [10] provided a revised structural model for $KHSi_2O_5{:}3H_2O$ gel which involves distorted silicate layers (Fig. 9) showing no distinct preferred orientational correlations beyond ~10 Å. The lack of long range ordering in both Furnas and Moxoto Dam ASR gels support that the water molecules are probably located in pores surrounding these kanemite-like fragments, as well as within the layers themselves.

4. Characterization of calcium–silicate–hydrates with PDF

Calcium–silicate–hydrate (C–S–H) is the most abundant phase in the matrix of portland cement concrete. Commonly referred to as the glue that holds concrete together, C–S–H is undoubtedly vital to the strength and durability of the hydrated cement matrix. Upon mixing of water and portland cement, C–S–H precipitates as clusters of nanoscale colloidal particles containing internal gel pores [72]. Several bulk properties of C–S–H are explained by the colloidal models proposed by Jennings [72,73]. These models posit the existence of a <50 Å diameter building block for C–S–H. In fact, the existence of such nanograins has long been suggested by neutron scattering [72], electron microscopy [74], and computer simulation studies [75]. Recently Skinner et al. [76], using high energy x-ray diffraction measurements, established that synthetic C–S–H (I) is nanocrystalline with a particle size of 35 Å (Fig. 11).

While the nanocrystallinity of C–S–H has been validated, there is still no consensus on its atomic structure despite decades of intensive research [77]. Currently accepted structural models use jennite ($Ca_9Si_6O_{10}(OH)_6.8H_2O$ [78], Ca/Si = 1.5) and 9 Å, 11 Å and 14 Å tobermorite crystal structures as starting points. Tobermorite is formed of a central sheet of calcium and oxygen atoms sandwiched by dreierketten silicate chains with possible additional water molecules and calcium atoms located in interlayer zones [79,80]. Molecular dynamics techniques can also provide new structural insight on C–S–H structure [75,81]; although, they tend to suggest more disorder in the nanograins.

Based on pair distribution analysis, Skinner et al. [76] have argued that C–S–H (I) is similar to a broadened 11 Å tobermorite. A detailed comparison of PDFs for C–S–H (I) and 11 Å tobermorite revealed remarkable similarities in the nearest neighbor environment. The PDF of C–S–H (I) (Fig. 11) illustrates the robust tetrahedral coordination of the Si–O (1.62 Å), and the presence of CaO_7 polyhedra (2.4 Å) on

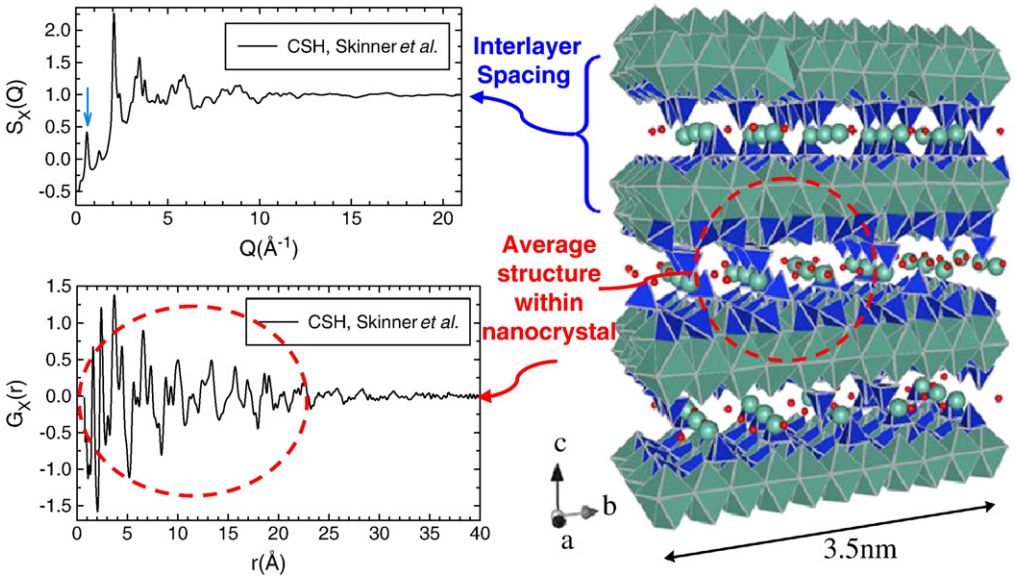

Fig. 11. (Left-top) x-ray structure factor $S_x(Q)$ of synthetic C–S–H (I) [76]. (Left-bottom) x-ray pair distribution function of synthetic C–S–H (I) has no correlated structure beyond 3.5 nm [76]. (Right) The molecular model of C–S–H (I) obtained by reverse Monte Carlo refinement. The initial structure is based on Hamid [79] 1.1 nm tobermorite crystal structure. The final structure is refined to be consistent with the measured data. Green polyhedral: CaO, blue tetrahedral: SiO, red spheres: inter layer O from water, green spheres: interlayer Ca [76].

average in C–S–H (I). The second neighbor Ca–O peak around 4–5 Å is a fingerprint for CaO sheet structure. The weak peak around 3 Å relates to Si–O–Si bonds in SiO_4 tetrahedra. The main difference between the crystalline structure and C–S–H (I) is in Si–Ca/Ca–Ca nearest neighbor correlations. Skinner et al. [76] pointed out that in order to match the C–S–H (I) measurement, the Ca–Ca separation must be broadened and shortened by 0.03–0.1 Å relative to the 11 Å tobermorite crystal structure. This results in a slight bend of the Ca–O sheet present in C–S–H (I) which may account for the finite length of Ca–O layers (unlike the infinitely long ones in tobermorite or jennite).

The new insights into the C–S–H (I) structure provided by the total scattering method motivated researchers to further pursue this approach. Taking advantage of the method, and inspired by mid-, near-, and far-infrared (IR) spectra studies of Yu et al. [82] on synthetic C–S–H with varying Ca/Si ratios, Soyer-Uzun et al. [83] conducted a systematic investigation on synthetic C–S–H with varying

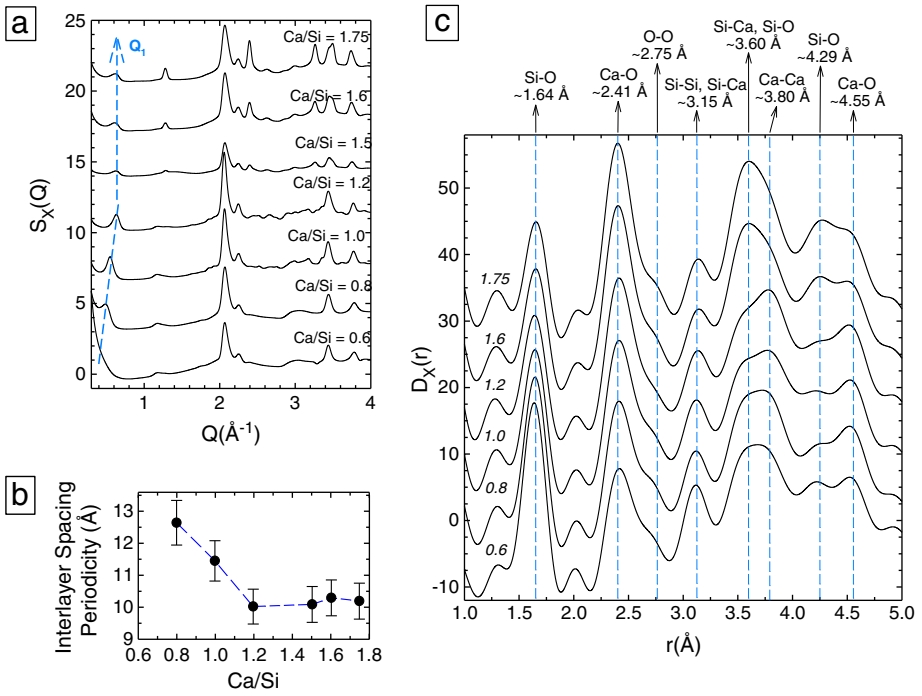

Fig. 12. (a) First sharp diffraction peak (Q_1) of the total x-ray structure factors $S_X(Q)$ of synthetic C–S–Hs with varying Ca/Si ratios (from 0.6 to 1.75). The Q-range for the plot is chosen 0.3–5.3 $Å^{-1}$ in order to make Q_1 more observable. The dashed line indicates the position Q_1 [83]. (b) The periodicity of interlayer space, $2\Pi/Q_1$. For Ca/Si = 0.8, the interlayer space is ~13 Å. It decreases to ~10 Å with decreased Ca/Si ratio, and remains constant around ~10 Å. [83] (c) Differential distribution functions, $D_x(r) = 4\pi r\rho_0[G_X(r) - 1]$, are obtained through Fourier transformation of $[S_X(Q)$ (data from [83]). Peaks are highlighted with dashed lines.

Ca/Si ratio (from 0.6 to 1.75). The first sharp diffraction peak (FSDP) at position Q_1 of the measured $S_X(Q)$ is correlated to periodicity of interlayer spacing by $2\Pi/Q_1$. The observed FSDPs (Fig. 12-a) and thus the periodicity of the interlayer spacing (Fig. 12-b) shows a strong dependence on the Ca/Si ratio of C–S–H. The interlayer spacing reduces from ~13 Å to ~10 Å with increasing Ca/Si ratio.

Changing the composition in a controlled manner also provides the opportunity to extract information from fairly complex PDFs of C–S–H. The major contributing correlations of C–S–H below 5 Å are given in Fig. 12-c. Peaks up to ~3 Å represent nearest neighbor environment in C–S–H. The peaks at ~1.66 Å and ~2.44 Å represent Si–O and Ca–O correlations. Si is tetrahedrally coordinated to O. The coordination of Ca_1–O_1 gradually decreases from ~7 to ~6, with increasing Ca/Si ratio following evolution from a 11 Å tobermorite-like (layers of 7-fold coordinated Ca-polyhedra) into a jennite-like (octahedral Ca environment) structure.

The detailed examination of next nearest neighbors reveals significant compositional changes at varying Ca/Si ratio. The ~3.6 Å and ~3.8 Å peaks are associated with Si–Ca/Si–O and Ca–Ca next nearest neighbors. For C–S–H with lower Ca/Si ratios the 3.8 Å peak is more intense compared to the 3.6 Å peak. A similar trend was observed between the at ~4.3 Å and ~4.6 Å peaks corresponding to longer range Si–O and Ca–O correlations. These compositional changes and loss of Ca-related correlations with increasing Ca/Si ratio in the PDFs may be related to Ca–O sheet distortion [83].

Pomies et al. [84] studied the speciation of cadmium in C–S–H using XRD, EXAFS and NMR. The EXAFS data were Fourier-transformed to obtain the pair distribution function. For the Cd-containing precipitated C–S–H, the first peak of the Fourier transform is related to the Cd–O contribution and the experiments indicate that Cd–O distance is not only slightly shorter than the Cd hydroxide, but also does not change with the Cd/Ca ratio. The best fit for the second peak in the Fourier transform at ~3.5 Å was obtained with a Ca shell a ~3.7 Å of the absorber for the Cd/Ca silicates.

5. Characterization of geopolymers with PDF

Geopolymers are synthetic aluminosilicate binders created by the alkali activation of aluminosilicate source materials with alkaline solutions. Industrial waste materials such as slag and fly ash can be a source of aluminosilicate raw materials, making geopolymers intrinsically environmentally attractive. Recently geopolymers have become an attractive alternative to traditional portland cement for certain applications; thus, the need for improved scientific characterization and optimization on geopolymers is steadily increasing. Reaction products of geopolymerization are cross-linked units of AlO_4 and SiO_4 tetrahedras with charge balancing alkali metal cations (such as K^+, Na^+) [85]. The products are mainly amorphous with a few aluminosilicate crystalline phases, depending on the synthesizing environment, *i.e.* pH value of alkali-activator, Si/Al ratio, and curing temperature, etc. [85,86]. In the past, the structure of geopolymers was identified with that of zeolitic precursors due to their similarities in the structure, at least in the short range order [85–88]. Detailed discussions of the nanostructural similarities between zeolites and fly ash geopolymers can be found in [89,90]. However, with 176 different types of zeolite present in the nature and each zeolite having slightly

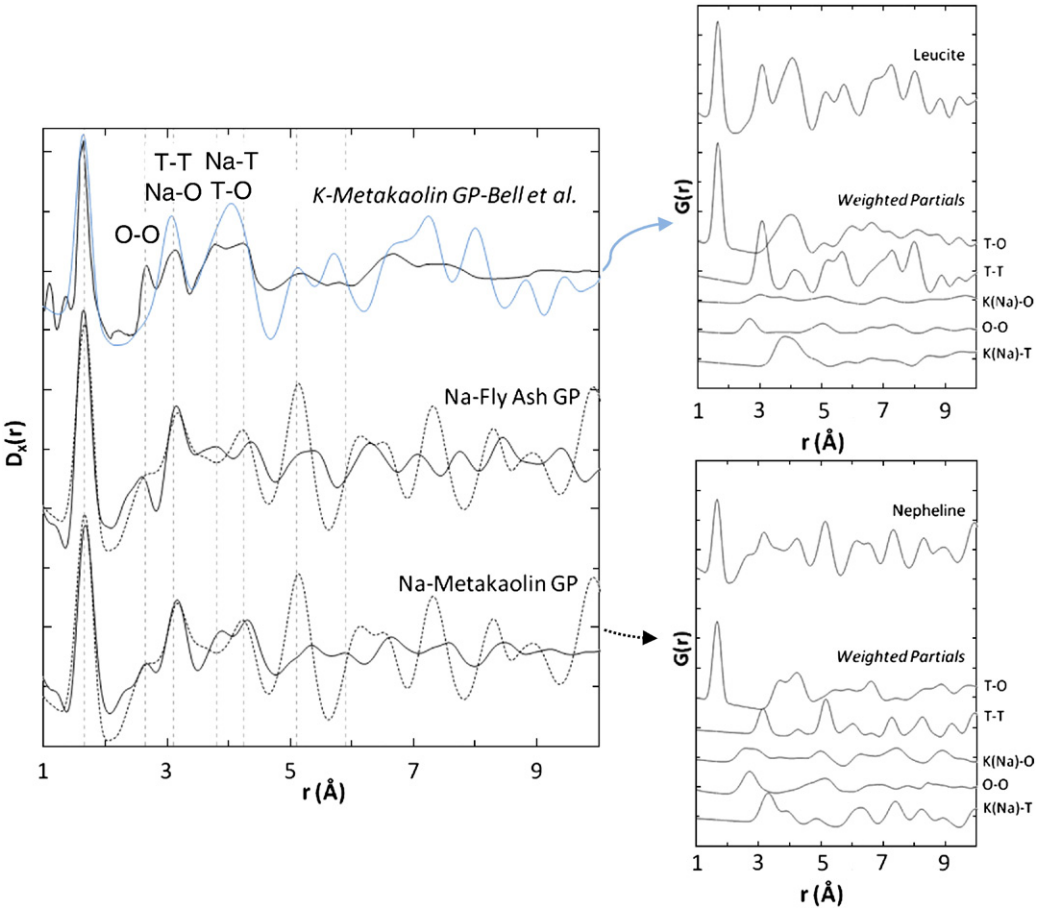

Fig. 13. (Left) The measured x-ray differential distribution functions for Na-Metakaolin, and Na-Fly ash geopolymers in comparison with PDF for K-Metakaolin geopolymer (measured by Bell et al. [93]), tetragonal leucite (blue — calculated from Dove et al. [94] with sratio = 0.7, and rcut = 2.5 on PDFGui) and nepheline (dotted — calculated from Hassan et al. [95] with sratio = 0.7, and rcut = 2.5) (Right) The atom specific weighted partial pair distributions for calculated leucite and nepheline.

different structural geometries, further detailed analysis is required to identify geopolymer structure. A recent synchrotron radiation diffraction study by Oh et al. [91] identified the disordered ABC-6 family of zeolites to be the most likely analog structure of zeolitic precursor for geopolymers (e.g., hydroxycancrinite and hydroxysodalite [44]) when fly ash is activated with high concentration NaOH or Na-silicate solution. Only 19 members among 176 zeolite species belong to an ABC-6 family of zeolite, and all members are structurally similar. Provis et al. [86] suggested a size limit of 8–10 nm (four unit cells) for nanocrystalline zeolites in geopolymers. Building on these results, a method to modify the structure of geopolymers at the molecular level to optimize and improve the mechanical properties of geopolymers is possible. In addition, manipulating the structure of geopolymers to increase their reactivity with toxic heavy metal ions to improve sequestration of contaminants can also be considered. Pair distribution function analysis of the geopolymers can be a powerful tool to search for the aforementioned possibilities.

Due to the heterogeneous nature of fly ash, the pair distribution analysis studies, as well as most of the other fundamental studies on geopolymers, initially focused on using pure metakaolin as an aluminosilicate source. The ability to convert metakaolin-based geopolymers to ceramics upon heating inspired Bell et al. [92] to conduct a series of PDF experiments on systematically heated Cs-metakaolin geopolymers. They found Cs-metakaolin geopolymer was resembling pollucite ($CsAlSi_2O_6$) up to ~9 Å. They also observed gradual formation of crystalline pollucite above 900 °C, and were able to provide a good fit with a cubic pollucite model on the PDF results on the heated Cs geopolymer. By tracking the changes in the T–T (tetrahedral Al or Si) correlation upon heating, Bell et al. [92] suggested that water was not mainly associated with Al–Si framework. In a second study, they continued investigating heated K-metakaolin geopolymer [93]. Using zeolitic tetragonal leucite ($KAlSi_2O_6.5.5H_2O$), they labeled the short range structural correlations for unheated K-metakaolin geopolymers.

Here we focused our interest on geopolymer samples using phase separated aluminosilicate glass obtained from fly ash F as a raw material. Table 1 lists the chemical compositions for the aluminosilicates used in the measurements. A comparison of Bell et al.'s [93] unheated K-geopolymer measurement (PDF) and with unheated Na-geopolymer measurements (D(r)) are shown in Fig. 13. Calculated leucite [94] and nepheline (a Na rich structure similar to leucite) [95] patterns (PDF) (using PDFGui [96]) are also shown in Fig. 13. It can be seen that for r<8 Å, the K-geopolymer from Bell et al.'s study resembled tetragonal leucite. However, this was not the case for our geopolymers, possibly due to unreacted raw aluminosilicates.

The measured structure factors for metakaolin and fly ash geopolymers are given in Fig. 14-a. Fig. 14-b shows D(r)s for aluminosilicates (raw materials) and their corresponding geopolymers. Fig. 14-c focuses on correlations up to 8 Å. The similar bond lengths for Si–O and Al–O often overlap resulting in one T–O peak where T = Si and Al in the PDF patterns. The Si–O bond is expected to be ~1.62 Å and tetrahedrally coordinated Al–O bond is ~1.75 Å. The first major peaks centered at ~1.66 Å for metakaolin-Na and at ~1.63 Å for fly ash F–Na geopolymers are related to the tetrahedrally coordinated Si–O and Al–O bond. This difference can be explained by the higher Al/Si ratio of metakaolin and/or some percentage of higher coordinate $AlO_{5,6}$ polyhedra. The low-r (up to 4 Å) region contains the average information on all Al and Si coordination polyhedras. In this short range region, our geopolymers resembled zeolitic nepheline. Beyond 4 Å, geopolymers show much weaker correlations compared to the refined nepheline model, most likely due to different connectivity of the polyhedra leading to the observed decreased medium range order.

The water environment in metakaolin geopolymers has been investigated in detail. It is concluded that relatively large amounts of water in metakaolin geopolymers reside in the large pores [97]. White et al. [98] took advantage of Neutron PDF analysis to investigate the state of water in K-metakaolin geopolymers. Upon systematical heating of K-geopolymer sample up to 1200 °C, they were able to confirm that a relatively small amount of water can exist in small pores, or as connected as hydroxyl groups to the Al–Si framework, and the majority of water is in large pores, or hydrating the charge-balancing cations associated with the Si–Al framework.

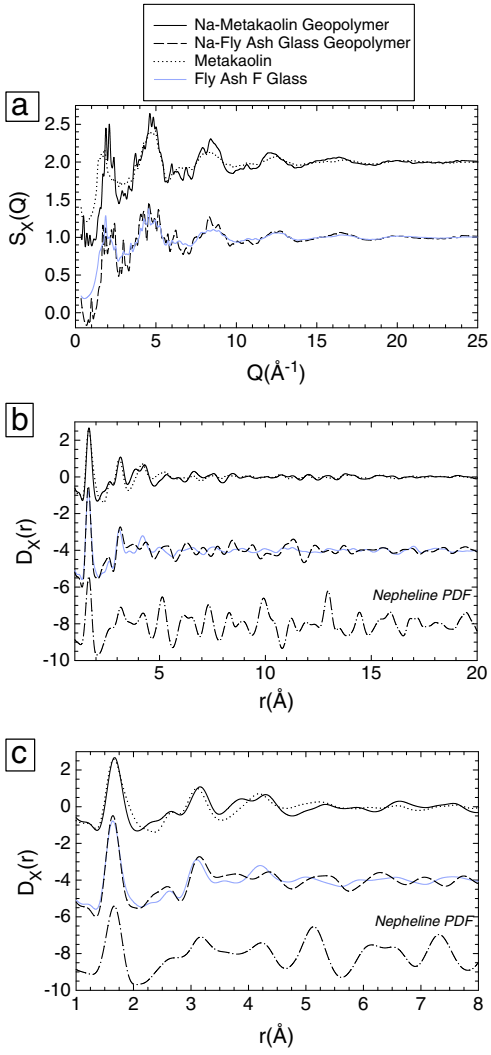

Fig. 14. (a) The measured $S_X(Q)$s for Na-geopolymers. (b–c) The measured x-ray differential distribution functions for aluminosilicates and their Na-geopolymers. The calculated nepheline PDF is also shown.

6. Conclusions and future directions

Many mineral admixtures for concrete, reactive aggregates, calcium–silicate hydrates, ASR gel and geopolymers have often varying degrees of disorder. Classical crystallographic characterization typically only determines the average structure of the material, while total scattering methods can provide insightful information about the local atomic arrangements. The resulting PDF data can also be used to validate MD simulations.

A PDF analysis of the total scattering of an ASR gel showed that although the local structure of the gel is similar to kanemite, the long-range structure of kanemite is lost in the ASR gel. The silicate layer structure is a much more disordered than predicted by molecular dynamics models. Total x-ray scattering measurements on synthetic C–S–H(I) shows nano-crystalline ordering with particle diameter 3.5 nm, similar to a size-broadened 1.1 nm tobermorite crystal structure. The largest difference between the tobermorite crystal

structure and C–S–H(I) is in the CaCa/CaSi nearest neighbor correlations. The slight bending of the Ca–O sheet may account for the limited size of the nano-crystalline particles.

There may many opportunities for future directions in extending the use of PDF for elucidating the structure of cementious materials: For example (i) following time resolved structural evolution of reaction processes (see reference [99]) (ii) combining x-ray and neutron PDF and/or PDF with EXAFS and/or NMR using modeling techniques like RMC to provide a highly constrained and therefore realistic atomic models, and (iii) deciphering the effect of pressure on the structure of materials [100].

Acknowledgments

This work was supported by the U.S. DOE, Argonne National Laboratory under contract number DE-AC02-06CH11357. This publication was based on work supported in part by Award No. KUS-l1-004021, made by King Abdullah University of Science and Technology (KAUST) and by NIST Grant 60NANB10D014. Also, thanks to Dr. L.B. Skinner, Dr. C. Erdonmez, Dr. B. Ercan, Dr. S. Soyer-Uzun and Dr. C. White for their valuable discussions during the production of this paper.

References

[1] G.L. Clark, D.H. Reynolds, Quantitative analysis of mine dusts: an X-Ray diffraction method, Industrial and Engineering Chemistry 8 (1936) 36–40.
[2] H.M. Rietveld, A profile refinement method for nuclear and magnetic structures, Journal of Applied Crystallography 2 (1969) 65–71.
[3] R.J. Hill, C.J. Howard, Quantitative phase analysis from neutron powder diffraction data using the Rietveld method, Journal of Applied Crystallography 20 (1987) 467–474.
[4] G. Le Saoût, V. Kocaba, K. Scrivener, Application of the Rietveld method to the analysis of anhydrous cement, Cement and Concrete Research 41 (2011) 133–148.
[5] K. Scrivener, Quantitative study of portland cement hydration by X-ray diffraction/Rietveld analysis and independent methods, Cement and Concrete Research 34 (2004) 1541–1547.
[6] T. Proffen, S.J.L. Billinge, T. Egami, D. Louca, Structural analysis of complex materials using the atomic pair distribution function — a practical guide, Zeitschrift Für Kristallographie 218 (2003) 132–143.
[7] A.C. Wright, Neutron scattering from vitreous silica. V. The structure of vitreous silica: what have we learned from 60 years of diffraction studies? Journal of Journal of Non-Crystalline Solids 179 (1994) 84–115.
[8] T. Egami, S.J.L. Billinge, Underneath the Bragg peaks: structural analysis of complex materials, Elsevier Ltd, 2003.
[9] H.E. Fischer, A.C. Barnes, P.S. Salmon, Neutron and x-ray diffraction studies of liquids and glasses, Reports on Progress in Physics 69 (2006) 233–299.
[10] C.J. Benmore, P.J.M. Monteiro, The structure of alkali silicate gel by total scattering methods, Cement and Concrete Research 40 (2010) 892–897.
[11] D.A. Keen, A comparison of various commonly used correlation functions for describing total scattering, Journal of Applied Crystallography 34 (2001) 172–177.
[12] X. Qiu, J.W. Thompson, S.J.L. Billinge, PDFgetX2: a GUI-driven program to obtain the pair distribution function from X-ray powder diffraction data, Journal of Applied Crystallography 37 (2004) 678.
[13] P.A. Egelstaff, Classic Fluids, in: D.L. Price, K. Skold (Eds.), Methods Of Experimental Physics, 1987, pp. 405–470.
[14] N. Cusack, The physics of structurally disordered matter, Hilger, Philadelphia, 1987.
[15] E. Lorch, Neutron diffraction by germania, silica and radiation-damaged silica glasses, Journal of Physics C-Solid State Physics 2 (1969) 229–237.
[16] C.B. Murray, C.R. Kagan, M.G. Bawendi, Synthesis and characterization of monodisperse nanocrystals and closed-packed nanocrystal assemblies, Annual Review of Materials Science 30 (2000) 545–610.
[17] B. Warren, H. Krutter, O. Morningstar, Fourier analysis of X-ray patterns of vitreous SiO_2 and B_2O_2, Journal of American Ceramic Society 19 (1936) 202–206.
[18] Q. Mei, C.J. Benmore, R. Sharma, J.L. Yarger, Intermediate range order in vitreous silica from a partial structure factor analysis, Physical Review B 78 (2008) 1–7.
[19] S.J.L. Billinge, I. Levin, The problem with determining atomic structure at the nanoscale, Science 316 (2007) 561–565 (New York, N.Y.).
[20] R.L. McGreevy, Reverse Monte Carlo modelling, Journal of Physics-Condensed Matter 13 (2001) R877.
[21] A.K. Soper, Partial structure factors from disordered materials diffraction data: an approach using empirical potential structure refinement, Physical Review B 72 (2005) 1–12.
[22] I. Bonhoure, I. Baur, E. Wieland, C. Johnson, A. Scheidegger, Uptake of Se(IV/VI) oxyanions by hardened cement paste and cement minerals: an X-ray absorption spectroscopy study, Cement and Concrete Research 36 (2006) 91–98.
[23] M. Vespa, R. Dähn, D. Grolimund, E. Wieland, A.M. Scheidegger, Co speciation in hardened cement paste: a macro- and micro-spectroscopic investigation, Environmental Science & Technology 41 (2007) 1902–1908.
[24] I. Bonhoure, E. Wieland, A.M. Scheidegger, M. Ochs, D. Kunz, EXAFS study of Sn (IV) immobilization by hardened cement paste and calcium silicate hydrates, Environmental Science & Technology 37 (2003) 2184–2191.
[25] K. Garbev, P. Stemmermann, L. Black, C. Breen, J. Yarwood, B. Gasharova, Structural features of C–S–H(I) and its carbonation in air-A Raman spectroscopic study. Part I: fresh phases, Journal of American Ceramic Society 90 (2007) 900–907.
[26] L. Black, C. Breen, J. Yarwood, K. Garbev, P. Stemmermann, B. Gasharova, Structural features of C–S–H(I) and its carbonation in air — a Raman spectroscopic study. Part II: carbonated phases, Journal of American Ceramic Society 90 (2007) 908–917.
[27] G.M. Bowers, R.J. Kirkpatrick, Natural abundance ^{43}Ca NMR spectroscopy of tobermorite and jennite: model compounds for C–S–H, Journal of American Ceramic Society 92 (2009) 545–548.
[28] A.V. Girão, I.G. Richardson, R. Taylor, R.M.D. Brydson, Composition, morphology and nanostructure of C–S–H in 70% white portland cement — 30% fly ash blends hydrated at 55 °C, Cement and Concrete Research 40 (2010) 1350–1359.
[29] U.S. Geological Survey, Mineral Commodity Summaries, Cement Statistics and Information, Washington, D.C., 2010, available at, http://minerals.usgs.gov/minerals/pubs/commodity/cement.
[30] P.K. Mehta, P.J.M. Monteiro, Concrete: Microstructure, Properties, and Materials, 2006.
[31] World Business Council for Sustainable Development The Cement Sustainability Initiative, Cement Industry Energy and CO_2 Performance: Getting the Numbers Right, 2009, p. 44.
[32] G. Marland, T.A. Boden, R.J. Andres, Global, Regional, and National CO_2 Emissions, Trends: A Compendium of Data on Global Change. Carbon Dioxide Information Analysis Center, Oak Ridge National Laboratory, U.S. DOE, Oak Ridge, TN, 2008, Available at, http://cdiac.ornl.gov/trends/emis/meth_reg.html.
[33] H.J. Feuerborn, Coal Ash Utilisation over the World and in Europe, Workshop On Environmental and Health Aspects Of Coal Ah Utilization, Israel, 2005.
[34] D.-zuo Cao, E. Selic, J.-D. Herbell, Utilization of fly ash from coal-fired power plants in China, Journal of Zhejiang University — Science A (2008) 681–687.
[35] Estimated based on information made available by the International Iron and Steel Institute (global iron production, 2008) and the U.S. Federal Highway Administration (blast furnace slag as a percentage of iron production) Available at, http://www.tfhrc.gov/hnr20/recycle/waste/bfs1.htm2008.
[36] B. Lothenbach, K. Scrivener, R.D. Hooton, Supplementary cementitious materials, Cement and Concrete Research 41 (2011) 217–229.
[37] W.H. Zachariasen, The atomic arrangement in glass, Journal of American Chemical Society 54 (1932) 3841–3851.
[38] P.K. Mehta, Siliceous ashes and hydraulic cements prepared therefrom — US Patent 4,105,459, 1978.
[39] P.K. Mehta, Highly durable cement products containing siliceous ashes — US Patent 5,346,548, 1994.
[40] P.K. Mehta, K.J. Folliard, Rice husk ash — a unique supplementary cementing material: durability aspects, ACI Special Publications SP-154 (1995) 531–542.
[41] H. Hamdan, M. Muhid, S. Endud, E. Listiorini, Z. Ramli, Si-29 MAS NMR, XRD and FESEM studies of rice husk silica for the synthesis of zeolites, Journal of Non-Crystalline Solids 211 (1997) 126–131.
[42] S. Kohara, K. Suzuya, High-energy X-raydiffraction studies of disordered materials, Nuclear Instruments & Methods in Physics Research B-Beam Interactions with Materials and Atoms 199 (2003) 23–28.
[43] P.K. Mehta, Global concrete industry sustainability, Concrete International 31 (2009) 45–48.
[44] J.E. Oh, J. Moon, M. Mancio, S.M. Clark, P.J.M. Monteiro, Bulk modulus of basic sodalite, $Na_8[AlSiO_4]_6(OH)2\cdot 2H_2O$, a possible zeolitic precursor in coal-fly-ash-based geopolymers, Cement and Concrete Research 41 (2011) 107–112.
[45] V.V. Hoang, Composition dependence of static and dynamic heterogeneities in simulated liquid aluminum silicates, Physical Review B 75 (2007) 1–15.
[46] S.H. Risbud, R.J. Kirkpatrick, A.P. Taglialavore, B. Montez, Solid-state NMR evidence of 4-, 5-, and 6-fold aluminum sites in roller-quenched SiO2–Al2O3 glasses, Journal of American Ceramic Society 70 (1987) C10–C12.
[47] M. Schmücker, H. Schneider, K.J.D. Okuno, M. MacKenzie, Comparative 27Al NMR and LAXS studies on rapidly quenched aluminosilicate glasses, Journal Of European Ceramic Society 19 (1999) 99–103.
[48] R. Weber, S. Sen, R.E. Youngman, R.T. Hart, C.J. Benmore, Structure of high alumina content Al2O3–SiO2 composition glasses, Source (2008) 16726–16733.
[49] M. Okuno, N. Zotov, Structure of SiO2–Al2O3 Glasses: Combined X-ray Diffraction, IR and Raman Studies, Journal of Non-Crystalline Solids 351 (2005) 1032–1038.
[50] S. Sen, R.E. Youngman, High-resolution multinuclear NMR structural study of binary aluminosilicate and other related glasses, Journal of Physical Chemistry B 108 (2004) 7557–7564.
[51] A. Winkler, J. Horbach, W. Kob, K. Binder, Structure and diffusion in amorphous aluminum silicate: a molecular dynamics computer simulation, Journal of Chemical Physics 120 (2004) 384–393.
[52] P. Pfleiderer, J. Horbach, K. Binder, Structure and transport properties of amorphous aluminium silicates: computer simulation studies, Chemical Geology 229 (2006) 186–197.

[53] V.V. Hoang, N.N. Linh, N.H. Hung, Structure and dynamics of liquid and amorphous Al2O3.2SiO2, The European Physical Journal - Applied Physics. 37 (2007) 111–118.
[54] N.N. Linh, V.V. Hoang, Structural properties of simulated liquid and amorphous aluminium silicates, Physica Scripta 76 (2007) 165–172.
[55] J. Ambroise, S. Martin-Calle, J. Pera, Pozzolanic behavior of thermally activated kaolin, ACI Special Publications SP-132 (1992) 731–748.
[56] B. Sabir, S. Wild, J. Bai, Metakaolin and calcined clays as pozzolans for concrete: a review, Cement and Concrete Composites 23 (2001) 441–454.
[57] C.E. White, J.L. Provis, T. Proffen, D.P. Riley, J.S.J. van Deventer, Combining density functional theory (DFT) and pair distribution function (PDF) analysis to solve the structure of metastable materials: the case of metakaolin, Physical Chemistry Chemical Physics PCCP. 12 (2010) 3239–3245.
[58] C.E. White, J.L. Provis, T. Proffen, D.P. Riley, J.S.J. van Deventer, Density functional modeling of the local structure of kaolinite subjected to thermal dehydroxylation, Journal of Physical Chemistry 114 (2010) 4988–4996.
[59] S. Sperinck, P. Raiteri, N. Marks, K. Wright, Dehydroxylation of kaolinite to metakaolin — a molecular dynamics study, Journal of Materials Chemistry (2010) 2118–2125.
[60] P. Monteiro, K. Wang, G. Sposito, M.C. Santos, W.P. de Andrade, Influence of mineral admixtures on the alkali-aggregate reaction, Cement and Concrete Research 27 (1997) 1899–1909.
[61] M. Prezzi, P.J.M. Monteiro, G. Sposito, The Alkali–Silica Reaction, Part I: Use of the Double-Layer Theory to Explain the Behavior of Reaction-Product Gels, ACI Materials Journal, 1997.
[62] M. Prezzi, P.J.M. Monteiro, G. Sposito, Alkali–silica reaction; Part 2: the effect of chemical additives, ACI Materials Journal 95 (1998).
[63] X. Hou, R.J. Kirkpatrick, L.J. Struble, P.J.M. Monteiro, Structural investigations of alkali silicate gels, Journal of American Ceramic Society 88 (2005) 943–949.
[64] C. Tambelli, J. Schneider, N. Hasparyk, P.J.M. Monteiro, Study of the structure of alkali–silica reaction gel by high-resolution NMR spectroscopy, Journal of Non-Crystalline Solids 352 (2006) 3429–3436.
[65] W. Wieker, C. Hubert, D. Deidemann, R. Ebert, Alkali–silica reaction — a problem of the insufficient fundamental knowledge of its chemical base, Materials Science of Concrete Special Volume (Sidnet Diamond Symposium) (1998) 395–408.
[66] W. Wieker, C. Hubert, Some experiences in chemical modelling of the alkali–silica reaction, 11th International Conference On alkali-aggregate Reaction, 2000, pp. 119–128.
[67] R.J. Kirkpatrick, A.G. Kalinichev, X. Hou, L. Struble, Experimental and molecular dynamics modeling studies of interlayer swelling: water incorporation in kanemite and ASR gel, Materials and Structures 38 (2005) 449–458.
[68] J. Du, L. Corrales, Compositional dependence of the first sharp diffraction peaks in alkali silicate glasses: a molecular dynamics study, Journal of Non-Crystalline Solids 352 (2006) 3255–3269.
[69] S.R. Elliott, Origin of the first sharp diffraction peak in the structure factor of covalent glasses and liquids, Journal of Physics-Condensed Matter 4 (1992) 7661–7678.
[70] P.S. Salmon, R.a. Martin, P.E. Mason, G.J. Cuello, Topological versus chemical ordering in network glasses at intermediate and extended length scales, Nature 435 (2005) 75–78.
[71] R.D. Shannon, C.T. Prewitt, Effective ionic radii in oxides and fluorides, Acta Crystallographica Section B - Structural Crystallography and Crystal Chemistry. 25 (1969) 925–946.
[72] A.J. Allen, J.J. Thomas, H.M. Jennings, Composition and density of nanoscale calcium–silicate–hydrate in cement, Nature Materials 6 (2007) 311–316.
[73] J.J. Thomas, A.J. Allen, H.M. Jennings, Structural changes to the calcium–silicate–hydrate gel phase of hydrated cement with age, drying, and resaturation, Journal of American Ceramic Society 91 (2008) 3362–3369.
[74] X. Zhang, W. Chang, T. Zhang, C.K. Ong, Nanostructure of calcium silicate hydrate gels in cement paste, Journal of American Ceramic Society 83 (2000) 2600–2604.
[75] R.J.-M. Pellenq, A. Kushima, R. Shahsavari, K.J. Van Vliet, M.J. Buehler, S. Yip, et al., A realistic molecular model of cement hydrates, Proceedings of National Academy of Sciences of US of America 106 (2009) 16102–16107.
[76] L.B. Skinner, S.R. Chae, C.J. Benmore, H.R. Wenk, P.J.M. Monteiro, Nanostructure of calcium silicate hydrates in cements, Physical Review Letters 104 (2010) 1–4.
[77] I.G. Richardson, The calcium silicate hydrates, Cement and Concrete Research 38 (2008) 137–158.
[78] E. Bonaccorsi, S. Merlino, H.F.W. Taylor, The crystal structure of jennite, $Ca_9Si_6O_{18}(OH)_6.8H_2O$, Cement and Concrete Research 34 (2004) 1481–1488.
[79] S.A. Hamid, Crystal structure of the 11 Å natural tobermorite $Ca_{2.25}[Si_3O_{7.5}(OH)_{1.5}].1H_2O$, Zeitschrift Für Kristallographie 154 (1981) 189–198.
[80] N. Lequeux, A. Morau, S. Philippot, P. Boch, Extended X-ray absorption fine structure investigation calcium silicate hydrates, Journal of American Ceramic Society 306 (1999) 1299–1306.
[81] H. Manzano, A. Ayuela, J.S. Dolado, On the formation of cementitious C–S–H nanoparticles, Journal of Computer Aided Materials Design 14 (2007) 45–51.
[82] P. Yu, R.J. Kirkpatrick, B. Poe, P.F. McMillan, X. Cong, Structure of calcium silicate hydrate (C–S–H): near-, mid-, and far-infrared spectroscopy, Journal of American Ceramic Society 82 (1999) 742–748.
[83] S. Soyer-Uzun, S.R. Chae, C.J. Benmore, H.-R. Wenk, P.J.M. Monteiro, Investigation on compositional evolution of calcium silicate, (2011) 1–20.
[84] M. Pomiès, N. Lequeux, P. Boch, Speciation of cadmium in cement Part I. Cd^{2+} uptake by C–S–H, Cement and Concrete Research 31 (2001) 563–569.
[85] J. Davisovits, Geopolymers: inorganic polymeric new materials, Journal of Thermal Analysis 37 (1991) 1633–1656.
[86] J.L. Provis, G.C. Lukey, J.V. Deventer, Do geopolymers actually contain nanocrystalline zeolites? A reexamination of existing results, Chemistry of Materials (2005) 3075–3085.
[87] D. Khale, R. Chaudhary, Mechanism of geopolymerization and factors influencing its development: a review, Journal of Materials Science 42 (2007) 729–746.
[88] A. Palomo, M.W. Grutzeck, M.T. Blanco, Alkali-activated fly ashes a cement for the future, Cement and Concrete Research 29 (1999) 1323–1329.
[89] P. Duxson, A. Fernández-Jiménez, J.L. Provis, G.C. Lukey, A. Palomo, J.S.J. Deventer, Geopolymer technology: the current state of the art, Journal of Materials Science 42 (2006) 2917–2933.
[90] Á. Palomo, S. Alonso, A. Fernandez-Jiménez, I. Sobrados, J. Sanz, Alkaline activation of fly ashes: NMR study of the reaction products, Journal of American Ceramic Society 87 (2004) 1141–1145.
[91] J.E. Oh, P.J.M. Monteiro, S.S. Jun, S. Choi, S.M. Clark, The evolution of strength and crystalline phases for alkali-activated ground blast furnace slag and fly ash-based geopolymers, Cement and Concrete Research 40 (2010) 189–196.
[92] J.L. Bell, P. Sarin, J.L. Provis, R.P. Haggerty, P.E. Driemeyer, P.J. Chupas, et al., Atomic structure of a cesium aluminosilicate geopolymer: a pair distribution function study, Chemistry of Materials 20 (2008) 4768–4776.
[93] J.L. Bell, P. Sarin, P.E. Driemeyer, R.P. Haggerty, P.J. Chupas, W.M. Kriven, X-ray pair distribution function analysis of a metakaolin-based, $KAlSi_2O_6 \cdot 5.5H_2O$ inorganic polymer (geopolymer), Journal of Materials Chemistry 18 (2008) 5974.
[94] M.T. Dove, T. Cool, D.C. Palmer, A. Putnis, E.K.H. Salje, B. Winkler, On the role of Al–Si ordering in the cubic-tetragonal phase transition in leucite, American Mineralogist 78 (1993) 486–492.
[95] I. Hassan, S.M. Antao, A.A.M. Hersi, Single-crystal XRD, TEM, and thermal studies of the satallite reflections nepheline, Canadian Mineralogist 41 (2003) 759–783.
[96] C.L. Farrow, P. Juhas, J.W. Liu, D. Bryndin, E.S. Božin, J. Bloch, et al., PDFfit2 and PDFgui: computer programs for studying nanostructure in crystals, Journal of Physics Condensed Matter 19 (2007) 335219.
[97] P. Duxson, G.C. Lukey, J.S.J. Deventer, Physical evolution of Na-geopolymer derived from metakaolin up to 1000 °C, Journal of Materials Science 42 (2007) 3044–3054.
[98] C.E. White, J.L. Provis, T. Proffen, J.S.J. Van Deventer, The effects of temperature on the local structure of metakaolin-based geopolymer binder: a neutron pair distribution function investigation, Journal of American Ceramic Society 93 (2010) 3486–3492.
[99] C.J. Benmore, J. Weber, M. Wilding, Temperature-dependent structural heterogeneity in calcium silicate liquids, Physical Review B 82 (2010) 224202.
[100] C.J. Benmore, E. Soignard, S. Amin, Structural and topological changes in silica glass at pressure, Physical Review B 81 (2010) 054105.
[101] D.L. Price, Neutron scattering from amorphous, disordered and nanocrystalline materials, Proceedings From the Meeting Of the School On Neutron Applications In Materials Science and Engineering Atomic Energy Of Canada, 1994.
[102] M.C. Wilding, M. Wilson, P.F. McMillan, Structural studies and polymorphism in amorphous solids and liquids at high pressure, Chemical Society Reviews 35 (2006) 964–986.